

1 **Entrainment and Dynamics of Ocean-derived Impurities within Europa's Ice**
2 **Shell**

3 **J. J. Buffo^{1,2}, B. E. Schmidt¹, C. Huber³, and C. C. Walker⁴**

4 ¹Georgia Institute of Technology ²Dartmouth College ³Brown University ⁴Woods Hole
5 Oceanographic Institution

6 Corresponding author: Jacob Buffo (jacob.j.buffo@dartmouth.edu)

7 **Key Points:**

- 8 • Planetary ices contain a chemical fingerprint of parent liquid reservoir thermochemical
9 properties and dynamics
- 10 • Observable thermochemical heterogeneities in Europa's ice shell can be used to infer the
11 geophysical evolution of the shell
- 12 • Constraining material entrainment and transport within planetary ices will aid in
13 assessing the habitability of ice-ocean worlds

14 **Abstract**

15 Compositional heterogeneities within Europa's ice shell likely impact the dynamics and
16 habitability of the ice and subsurface ocean, but the total inventory and distribution of impurities
17 within the shell is unknown. In sea ice on Earth, the thermochemical environment at the ice-ocean
18 interface governs impurity entrainment into the ice. Here, we simulate Europa's ice-ocean interface
19 and bound the impurity load (1.053-14.72 ppt bulk ice shell salinity) and bulk salinity profile of
20 the ice shell. We derive constitutive equations that predict ice composition as a function of the
21 interfacial thermal gradient and ocean composition. We show that evolving solidification rates of
22 the ocean and hydrologic features within the shell produce compositional variations (ice bulk
23 salinities of 5-50% of the ocean salinity) that can affect ice's material properties. These results
24 imply that ocean materials entrained within Europa's ice shell affect the formation of geologic
25 terrain and could be resolved by future spacecraft observations.

26 **Plain Language Summary**

27 Europa, the second innermost moon of Jupiter, likely houses an interior ocean that could provide
28 a habitat for life. This ocean resides beneath a ~10-30 km thick ice shell which could act as a
29 barrier or conveyor for ocean-surface interactions thought to play a crucial role in facilitating the
30 ocean's habitability. A key component of these ocean-surface interactions is the transport of ocean
31 derived materials through the shell. Additionally, these ocean-derived impurities likely play a
32 significant role in the geophysics of the moon's icy exterior. That said, little is known about the
33 interior properties of the ice shell or ocean. On Earth, the characteristics and properties of ocean-
34 derived ices are governed by their thermochemical environment at the time of their formation.
35 Here we extend models of sea ice to accommodate the Europa ice-ocean environment and produce
36 physically realistic predictions of Europa's ice shell composition and the thermochemical
37 evolution of water bodies (fractures and lenses) within the shell. These results provide a method
38 for relating observable ice characteristic to interior ocean properties and dynamics as well as a
39 predictive tool for simulating the evolution of Europa's ice shell and water bodies. This has direct
40 implications for assessing the moon's habitability, understanding the evolution of geophysical
41 structures within the ice shell, and the interpretation of upcoming mission data (e.g. ice penetrating
42 radar measurements made by Europa Clipper).

44 **1. Introduction**

45 Europa's ocean was the first detected beyond Earth [*Khurana et al.*, 1998; *Kivelson et al.*,
46 2000]. Studies [*Cassen et al.*, 1979; *R Pappalardo et al.*, 1999; *Ross and Schubert*, 1987; *Squyres*
47 *et al.*, 1983] indicate that Europa's internal structure hosts a thick global ocean bounded by a
48 silicate mantle below and a water ice shell above. These findings have fueled interest in the moon's
49 interior dynamics, which may facilitate environments suitable for life [*Board and Council*, 2012;
50 *Chyba and Phillips*, 2001; *Des Marais et al.*, 2008; *Reynolds et al.*, 1983; *Russell et al.*, 2017].
51 Europa's ice shell plays a crucial role in the moon's dynamics and evolution, as both a barrier and
52 conveyor between the ocean and surface. Because most of the data available for Europa is derived
53 from remote sensing techniques, the ice shell is a primary medium through which the properties
54 of the ocean and interior can be understood, as the ice expresses how the body has evolved through
55 its geology and composition. However, at present many of the ice shell's properties are not well
56 constrained, including ice thickness, ice chemistry, and the distribution of shallow water [*Billings*
57 *and Kattenhorn*, 2005; *Schmidt et al.*, 2011; *Walker and Schmidt*, 2015; *Mikhail Y Zolotov and*
58 *Shock*, 2001]. Locating potentially habitable niches, understanding the transport processes

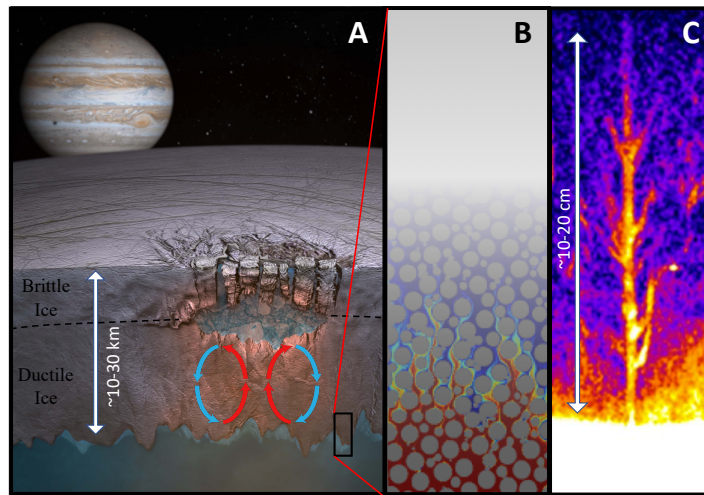
59 supporting them, investigating their connectivity, and constraining characteristics of the European
60 environment are planned objectives of the Europa Clipper mission currently under development
61 by NASA [Phillips and Pappalardo, 2014]. As such, quantifying the physical, thermal, chemical,
62 and mechanical properties of the ice shell is imperative to understanding Europa's geophysical and
63 material transport processes that control its habitability.

64 Heterogeneities in the ice shell have been linked to a number of proposed dynamic
65 processes: solid state convection in the lower ice shell [Han and Showman, 2005; Howell and
66 Pappalardo, 2018; McKinnon, 1999], subduction or subsumption of surface material [Johnson et
67 al., 2017b; Kattenhorn, 2018; Kattenhorn and Prockter, 2014], eutectic melting that may lead to
68 the formation of chaos and lenticulae [Manga and Michaut, 2017; Michaut and Manga, 2014;
69 Schmidt et al., 2011], formation and sustenance of water bodies within the shell [Kargel et al.,
70 2000; M Yu Zolotov and Kargel, 2009]. Yet the process by and rate at which impurities are
71 entrained within the ice remain poorly constrained, and while current models implement a range
72 of potential impurity loads to test model sensitivity to variations in ice composition [Han and
73 Showman, 2005; Johnson et al., 2017a; R T Pappalardo and Barr, 2004] they do not predict ice
74 composition directly. Furthermore, observations reveal that young, active terrain is richer in non-
75 ice material than the average ice [McCord et al., 2002] (Supplementary Figure S1), suggesting
76 recent interaction with subsurface water reservoirs enriched with salts [Manga and Michaut, 2017;
77 Michaut and Manga, 2014; Schmidt et al., 2011], the effusion of ocean materials through fractures
78 [Fagents, 2003], or melt through of a thin ice shell [Greenberg et al., 1999].

79 When ice forms in an aqueous environment, it preserves a thermochemical record of the
80 water from which it formed [Feltham et al., 2006; Hunke et al., 2011; Turner and Hunke, 2015].
81 For Europa, the ice shell grew from the freezing of, and is thus a window into, the ocean. With a
82 geologically young surface ($<10^8$ yr [Carr et al., 1998]) suggesting active ice shell overturn,
83 dynamic regions of Europa's surface (e.g. bands and chaos) may harbor 'fossil ocean material'
84 entrained in the ice shell as recently as 1Mya [Howell and Pappalardo, 2018]. This could provide
85 an accessible sample of the contemporary ocean, as it is highly likely that Europa's ice, much like
86 sea ice and marine ice on Earth, contains pockets and channels filled with brine, salts, gasses, and
87 other impurities derived from the dynamics of freezing at the ice-ocean interface [Eicken, 2003; R
88 T Pappalardo and Barr, 2004; M Yu Zolotov and Kargel, 2009; Zotikov et al., 1980] (See Figure
89 1). On Earth, sea ice captures such a record of the thermochemical processes in the upper ocean
90 during its formation [Buffo et al., 2018]. As the ocean solidifies, dissolved solutes are rejected as
91 crystalline ice forms and a porous water-ice matrix filled with hypersaline interstitial fluid is
92 produced [Buffo et al., 2018; Feltham et al., 2006; Hunke et al., 2011; Turner and Hunke, 2015].
93 This process produces a compositionally-driven gravitational instability in the newly formed
94 porous ice layer that results in buoyancy-driven convection of the denser pore fluid into the
95 underlying liquid reservoir. Referred to as gravity drainage, this process has been observed to be
96 the primary method of desalination during sea ice formation and has been successfully
97 incorporated into a number of numerical models [Buffo et al., 2018; Griewank and Notz, 2013;
98 Turner and Hunke, 2015; Wells et al., 2011].

99 Quantifying the relationship between Europa's ice composition and interfacial
100 thermochemistry at the time of formation would provide a technique for linking observed ice
101 properties to characteristics of its origin liquid water reservoir (a 'frozen fingerprint' of the source
102 water) and forecasting the properties of ice produced under diverse thermal and chemical
103 conditions – informing the synthesis of future mission data and geodynamic models. Impurities
104 and structural heterogeneities within ice alter its thermal, physicochemical, and dielectric

105 properties [Feltham *et al.*, 2006; Hunke *et al.*, 2011; Weeks and Ackley, 1986]. Thus, beyond the
 106 ice shell's chemistry, the dynamics of impurity entrainment will affect the potentially appreciable,
 107 and ongoing, hydrological activity within Europa's ice shell in the form of perched water lenses,
 108 fractures, dikes, and sills [Manga and Michaut, 2017; Michaut and Manga, 2014; Schmidt *et al.*,
 109 2011; Walker and Schmidt, 2015]. Moreover, interpretation of measurements taken by Europa
 110 Clipper's ice penetrating radar, REASON, depend critically on ice composition and dielectric
 111 properties [Kalousova *et al.*, 2017; Weeks and Ackley, 1986]. If the ice shell is impurity rich it has
 112 the potential to reflect and attenuate radar signals, which can be used to investigate the ice shell's
 113 interior structure but may also prevent observation of the ice-ocean interface [Kalousova *et al.*,
 114 2017].



130 **Figure 1 – The Europa ice-ocean system. A)** A brittle ice lithosphere overlies a ductile ice mantle (dashed line) in
 131 contact with a subsurface ocean. A diapir generated perched water lens is an example of a putative hydrological feature
 132 within the ice shell that may facilitate the surface expression of recently entrained ocean material. **B)** Akin to terrestrial
 133 environments, the ice-ocean interface of Europa will likely be characterized by a two-phase ice-brine system, allowing
 134 solutes and other ocean material to be trapped within pore spaces. **C)** Brine channels in terrestrial sea ice. (Image
 135 Credit: A – Adapted from Britney Schmidt/Dead Pixel FX, UT Austin. B – Adapted from Joaquín Jiménez-Martínez
 136 http://petrelharp.github.io/asn_2016/asn-2016-talk.html C – Adapted from [Worster and Rees Jones, 2015])

137
 138 To constrain the impurity load within Europa's ice shell and investigate the possible
 139 dynamics associated with the presence of salt in the ice shell, we constructed a one-dimensional
 140 reactive transport model adapted from the sea ice model of [Buffo *et al.*, 2018] for the Europa
 141 environment. We performed simulations of the formation and evolution of Europa's ice shell,
 142 validated against empirical observations of sea ice and marine ice growth rates and composition.
 143 The simulations include fluid and solute transport and the associated impurity entrainment that
 144 occurs at ice-ocean/brine interfaces. The model actively tracks the dynamic ice-ocean/brine
 145 interface as it propagates and catalogs the composition of the ice as it becomes impermeable and
 146 traps solutes within the ice. Since the ice composition derives from the initial ocean, we test an
 147 array of putative European ocean chemistries and thermal regimes and derive constitutive
 148 relationships between entrainment rates and the local thermal and chemical environment.

149 150 **2. Methods**

151 2.1 Numerical Model

152 The growth and evolution of the ice-ocean/brine interface is treated using an adapted
 153 version of the one-dimensional, two-phase, reactive transport model of sea ice described by [Buffo
 154 *et al.*, 2018]. Water/ice mass, energy, and salinity are conserved using a coupled set of equations
 155 that combines mushy layer theory and the enthalpy method. The governing equations are:

$$156 \quad \bar{\rho}c \frac{\partial T}{\partial t} = \left(\bar{k} \frac{\partial^2 T}{\partial z^2} \right) - \rho_{ice} L \frac{\partial \phi}{\partial t} \quad (1)$$

$$157 \quad \phi \frac{\partial S_{br}}{\partial t} = \left(\bar{D} \frac{\partial^2 S_{br}}{\partial z^2} \right) - \frac{\rho_{ice}}{\rho_{br}} S_{br} \frac{\partial \phi}{\partial t} \quad (2)$$

$$158 \quad H = c_{ice} T + L\phi \quad (3)$$

$$159 \quad \phi = \begin{cases} 0 & H < H_s = c_{ice} T_m \\ (H - H_s)/L & \text{if } - H_s \leq H \leq H_s + L \\ 1 & H > H_s + L \end{cases} \quad (4)$$

160 where ρ is density, c is specific heat capacity, T is temperature, t is time, z is the vertical
 161 coordinate, k is heat conductivity, L is the latent heat of fusion for the water to ice phase
 162 transformation, ϕ is liquid fraction, S is salinity, D is salt diffusivity, H is enthalpy, H_s is the
 163 enthalpy of a discretization cell consisting of only solid ice, and T_m is melting/freezing
 164 temperature. Subscripts *ice* and *br* refer to characteristics of the ice and brine components of the
 165 two-phase mixture, respectively, and variables carrying an over bar are volumetrically averaged
 166 quantities (i.e. $\bar{y} = \phi y_{br} + (1 - \phi) y_{ice}$). Equations 1 and 2 ensure conservation of heat and mass,
 167 respectively, and equations 3 and 4, combined, make up the enthalpy method. All variables and
 168 values used throughout the text can be found in Table 1.

169 The desalination of forming ice is governed by brine expulsion and gravity drainage. Brine
 170 expulsion refers to the phase change driven flux of hypersaline brine within the porous ice matrix
 171 into the underlying liquid reservoir. As a volume containing both ice and brine components
 172 continues to solidify, assuming incompressible flow, conservation of mass requires that brine must
 173 be expelled from the volume. This is due to the density difference between ice and water. Given
 174 the unidirectional solidification scenarios considered here, the brine will move downward into the
 175 ambient ocean/brine. Gravity drainage refers to the buoyancy-driven convective overturn of brine
 176 within the permeable multiphase layer. Both effects were considered by the model of Buffo *et al.*
 177 (2018); however, in line with previous research [Griewank and Notz, 2013; Wells *et al.*, 2011],
 178 gravity drainage was shown to be the primary mode of desalination. As such, with minimal loss
 179 of accuracy, we forego simulating phase change driven Darcy flow (brine expulsion) in the porous
 180 ice and opt to use the one-dimensional gravity drainage parameterization of [Griewank and Notz,
 181 2013] to represent fluid transport. This parameterization represents the process of gravity drainage
 182 through brine channels as a linear function of the local Rayleigh number, and is widely used for
 183 solving multiphase melting/solidification problems [Griewank and Notz, 2013; Turner and Hunke,
 184 2015; Turner *et al.*, 2013; Wells *et al.*, 2011]. Here, the mass of brine transported out of a
 185 multiphase layer j is given as:

191

192

$$br_j^\downarrow = \alpha(Ra_j - Ra_c)dz^3dt = \alpha\left(\frac{g\rho_{sw}\beta\Delta S_j\tilde{\Pi}h_j}{\kappa\mu} - Ra_c\right)dz^3dt \quad (5)$$

193

194

195

196

197

198

199

200

201

202

203

204

205

206

where α is a constant of proportionality, Ra_j is the Rayleigh number of the j th layer, Ra_c is the critical Rayleigh number, dz and dt are the spatial and temporal discretization sizes, respectively, g is acceleration due to gravity, ρ_{sw} is the density of the ambient reservoir fluid (ocean/brine), β is a density coefficient describing the relationship between density and salinity, ΔS_j is the difference in salinity of the brine from ambient fluid, h_j is the height of the j th layer above the basal surface of the ice, κ is the thermal diffusivity of seawater, μ is the kinematic viscosity of seawater, and $\tilde{\Pi}_j$ is the minimum permeability of any layer between the j th layer and the basal ice surface. The permeability function given by Griewank and Notz (2013) is utilized, and a critical porosity cutoff is implemented to prevent drainage from layers containing low liquid fractions (here $\phi < 0.05$ [K M Golden et al., 2007] results in a layer's fluid transport being shut off). Heat and salt are transported out of the model domain by this convective process and the equations of mushy layer theory (Eq. 1 & 2) are modified accordingly (See [Buffo et al., 2018] for details).

Symbol	Definition	Value	Units
α	1D Advection Coefficient	1.56×10^{-1}	$\text{kg m}^{-3} \text{s}^{-1}$
β	Density (Salinity) Coefficient	5.836×10^{-4}	kg ppt^{-1}
$br^{\uparrow,\downarrow}$	Vertical Brine Transport	Calculated	kg
c_{br}	Brine Heat Capacity	3985	$\text{J kg}^{-1} \text{K}^{-1}$
c_{ice}	Ice Heat Capacity	2000	$\text{J kg}^{-1} \text{K}^{-1}$
D	Salt Diffusivity	Calculated	$\text{m}^2 \text{s}^{-1}$
g	Acceleration Due to Gravity	1.32/9.8	m s^{-2}
h	Distance to Interface	Calculated	m
H	Ice Shell Thickness	Varies	km
H	Enthalpy	Calculated	J kg^{-1}
H_S	Enthalpy of Solid Cell	Calculated	J kg^{-1}
k_{br}	Brine Heat Conductivity	0.6	$\text{W m}^{-1} \text{K}^{-1}$
k_{ice}	Ice Heat Conductivity	2	$\text{W m}^{-1} \text{K}^{-1}$
κ	Thermal Diffusivity	Varies	$\text{m}^2 \text{s}^{-1}$
L, L_f	Latent Heat of Fusion	334,774	J kg^{-1}
λ	Coefficient Dependent on St	Calculated	-
μ	Kinematic Viscosity	1.88×10^{-3}	$\text{m}^2 \text{s}^{-1}$
ϕ	Liquid Fraction	Calculated	-
ϕ_c	Critical Porosity	0.05	-
Π	Permeability	Calculated	m^2
Ra	Rayleigh Number	Calculated	-
Ra_c	Critical Rayleigh Number	1.01×10^{-2}	-
ρ_{br}	Brine Density	Varies	kg m^{-3}
ρ_{ice}	Ice Density	917	kg m^{-3}
ρ_{sw}	Ocean/Reservoir Density	Varies	kg m^{-3}
S	Salinity	Calculated	ppt
S_{lim}	Minimum Salinity	Varies	ppt
S_{oc}	Ocean/Reservoir Salinity	Varies	ppt
S_{tot}	Bulk Salinity/Total Salt	Calculated	ppt
St	Stefan Number	Calculated	-
t	Time	-	s
T	Temperature	Calculated	K

T_0	Supercooled Temperature	Varies	K
T_1	Liquid Temperature	Varies	K
T_m	Melting/Freezing Temperature	Varies	K
T_{oc}	Ocean Temperature	Varies	K
T_s	Surface Temperature	100	K
v_m	Freezing Front Velocity	Calculated	m s ⁻¹
x_m	Freezing Front Position	Calculated	m
z	Vertical Coordinate	-	m

Table 1 – Variables. All variables used in the text, along with their definition, values, and units.

2.2 The Stefan Problem: Deriving the Constitutive Equations

The interpolation of results used to derive the constitutive relationships between ice characteristics and the thermochemical environment hinges on the ability to fit the simulated data to a predefined function. The form of this function should be representative of the physical processes occurring within the simulation. As the equations governing the multiphase reactive transport model do not lend themselves to an analytical solution, it is logical to seek a simplified system that does. To investigate the evolution of dissolved salt in an ice-ocean environment we make a number of simplifying assumptions and solve Equation 2 analytically.

The classic Stefan problem describes the dynamics and evolution of pure substance melting/solidification and is well documented in the literature [Huber *et al.*, 2008; Michaut and Manga, 2014; Rubinštejn, 2000]. The basic geometry of the problem can be seen in Supplementary Figure S2. In 1860 Carl Neumann found the analytical solution of the thermal profile in the solid and the time dependent solidification front to be [Huber *et al.*, 2008]:

$$T(x, t) = T_0 - (T_0 - T_1) \frac{\operatorname{erf}\left(\frac{x}{2\sqrt{\kappa t}}\right)}{\operatorname{erf}(\lambda)} \quad (6)$$

$$x_m(t) = 2\lambda\sqrt{\kappa t} \quad (7)$$

$$\lambda \exp(\lambda^2) \operatorname{erf}(\lambda) = \frac{St}{\sqrt{\pi}} = \frac{c(T_0 - T_1)}{L_f\sqrt{\pi}} \quad (8)$$

where $T(x, t)$ is the temperature within the solid at position x and time t , T_0 is the temperature at the undercooled surface and is lower than the melting temperature of the solid, T_1 is the temperature of the liquid, κ is the thermal diffusivity of the solid, x_m is the position of the solidification front, λ is a coefficient depending on St , erf is the error function, St is the Stefan number defined as $St = c(T_0 - T_1)/L_f$, c is the specific heat of the solid, and L_f is the latent heat of fusion for the water-ice phase transition.

While the Stefan problem represents a simpler system than that of our reactive transport model, the underlying physics governing solidification are the same and similar behavior is to be expected. It has been suggested that the amount of impurities entrained in forming ice is related to the rate at which the ice forms [Masayoshi Nakawo and Sinha, 1984; Weeks and Ackley, 1986; M Yu Zolotov and Kargel, 2009]. Equations 6-8 can be utilized to investigate the relationships between the rate of ice formation and both the freezing front position and local thermal gradient. First, differentiating Equation 7 with respect to time gives:

242

$$v_m(t) = \dot{x}_m(t) = \frac{\lambda\kappa}{\sqrt{\kappa t}} = \frac{2\lambda^2\kappa}{x_m(t)} \quad (9)$$

244

$$\Rightarrow v_m(t) \propto \frac{1}{x_m(t)} \quad (10)$$

246

247 where $v_m(t)$ is the solidification front velocity, which is equivalent to the rate of ice formation.

248 This suggests that the rate of ice formation is inversely proportional to the position of the

249 solidification front. Second, differentiating Equation 6 with respect to position gives:

250

$$\frac{\partial T(x, t)}{\partial x} = -\frac{(T_0 - T_1)}{\text{erf}(\lambda)} \frac{1}{\sqrt{\pi\kappa t}} \exp(-x^2/4\kappa t) \quad (11)$$

252

253 At the position of the solidification front, $x_m(t) = 2\lambda\sqrt{\kappa t}$, Equation 11 becomes:

254

255

$$\frac{\partial T(x_m, t)}{\partial x} = -\frac{(T_0 - T_1)}{\text{erf}(\lambda)} \frac{1}{\sqrt{\pi\kappa t}} \exp(-\lambda^2) \quad (12)$$

257

258 From Equation 9 we see that $\sqrt{\kappa t} = \lambda\kappa/v_m(t)$. Substituting this result into Equation 12 gives:

259

$$\frac{\partial T(x_m, t)}{\partial x} = -\frac{(T_0 - T_1)}{\text{erf}(\lambda)} \frac{1}{\sqrt{\pi}\lambda\kappa} \exp(-\lambda^2)v_m(t) \quad (13)$$

261

$$\Rightarrow \frac{\partial T(x_m, t)}{\partial x} \propto v_m(t) \quad (14)$$

263

264 Suggesting that the rate of ice formation is directly proportional to the local thermal gradient at the

265 solidification front. The relationships derived in Equations 10 & 14 provide insight into the

266 spatiotemporal evolution of the Stefan problem and its dependence on the local thermal

267 environment. These results will be utilized below, where a modified Stefan problem (inclusion of

268 a solute and fluid dynamics) is described and an analytical solution is derived. This solution

269 describes the spatial and temporal distribution of the solute and provides the functional form of

270 the constitutive equations used throughout the text.

271 To investigate the evolution of dissolved salt in an ice-ocean environment we make a

272 number of simplifying assumptions and solve Equation 2 analytically. Assuming top-down

273 unidirectional solidification of a salty ocean (e.g. sea ice, European ocean solidification) the

274 evolution of salt in the system can be described by the equations of reactive transport (Equation 2

275 including the gravity drainage parameterization, with br subscripts dropped from S terms for

276 simplicity):

277

$$\phi \frac{\partial S}{\partial t} = \left(\bar{D} \frac{\partial^2 S}{\partial z^2} \right) - \frac{\rho_{ice}}{\rho_{br}} S \frac{\partial \phi}{\partial t} + br_j^\downarrow \frac{\partial S}{\partial z} \quad (15)$$

279

280 where br_j^\downarrow is the brine velocity in the j th layer described by the one-dimensional gravity drainage
 281 parameterization. Introducing a new coordinate, ξ , such that $\xi = z - z_m(t)$, places the origin at
 282 the ice-ocean interface and constitutes a moving coordinate system. In this new coordinate system
 283 Equation 15 can be written as:

$$284 \quad \phi \frac{\partial S}{\partial \xi} \frac{\partial \xi}{\partial t} = \bar{D} \left[\frac{\partial^2 S}{\partial \xi^2} \left(\frac{\partial \xi}{\partial z} \right)^2 + \frac{\partial S}{\partial \xi} \frac{\partial^2 \xi}{\partial z^2} \right] - \frac{\rho_{ice}}{\rho_{br}} S \frac{\partial \phi}{\partial \xi} \frac{\partial \xi}{\partial t} + br_j^\downarrow \frac{\partial S}{\partial \xi} \frac{\partial \xi}{\partial z} \quad (16)$$

286
 287 Rearranging Equation 16:

$$288 \quad -\bar{D} \left[\frac{\partial^2 S}{\partial \xi^2} \left(\frac{\partial \xi}{\partial z} \right)^2 + \frac{\partial S}{\partial \xi} \frac{\partial^2 \xi}{\partial z^2} \right] - br_j^\downarrow \frac{\partial S}{\partial \xi} \frac{\partial \xi}{\partial z} + \phi \frac{\partial S}{\partial \xi} \frac{\partial \xi}{\partial t} = -\frac{\rho_{ice}}{\rho_{br}} S \frac{\partial \phi}{\partial \xi} \frac{\partial \xi}{\partial t} \quad (17)$$

290
 291 Taking the appropriate spatial and temporal derivatives of ξ and substituting their values into
 292 Equation 17 gives:

$$293 \quad -\bar{D} \frac{\partial^2 S}{\partial \xi^2} - (br_j^\downarrow + \phi v_m(t)) \frac{\partial S}{\partial \xi} = v_m(t) \frac{\rho_{ice}}{\rho_{br}} S \frac{\partial \phi}{\partial \xi} \quad (18)$$

294
 295 For simplicity, we assume that $\phi(\xi) = H(\xi)$, where $H(\xi)$ is the Heaviside step function. While
 296 this is indeed a simplification, as it represents the mushy layer as an infinitesimally thin regime,
 297 the general liquid fraction profile of evolving sea ice demonstrates similar structure (See Figures
 298 5-7 of Buffo et al., 2018). Substituting $\phi(\xi) = H(\xi)$ into Equation 18 results in a simplified
 299 conservation of mass equation in the moving coordinate system:

$$300 \quad -\bar{D} \frac{\partial^2 S}{\partial \xi^2} - (br_j^\downarrow + \phi v_m(t)) \frac{\partial S}{\partial \xi} = v_m(t) \frac{\rho_{ice}}{\rho_{br}} S \delta(\xi) \quad (19)$$

301
 302 where $\delta(\xi)$ is the delta function. Equation 19 can be solved using Fourier transforms. Let the
 303 transform variable be χ , such that:

$$304 \quad S(\chi) = \mathcal{FT}[S(\xi)] = \int_{-\infty}^{\infty} S(\xi) \exp(-i2\pi\chi\xi) d\xi \quad (20)$$

$$305 \quad S(\xi) = \mathcal{FT}^{-1}[S(\chi)] = \int_{-\infty}^{\infty} S(\chi) \exp(i2\pi\chi\xi) d\chi \quad (21)$$

306
 307 Applying the Fourier transform to Equation 19 gives:

$$308 \quad 4\pi^2 \chi^2 \bar{D} S(\chi) - i2\pi\chi (br_j^\downarrow + \phi v_m(t)) S(\chi) = v_m(t) \frac{\rho_{ice}}{\rho_{br}} S(\xi = 0, t) \quad (22)$$

309
 310 Equation 22 has the solution:

311
 312
 313
 314
 315
 316

$$S(\chi) = S(\chi, t) = \frac{v_m(t) \frac{\rho_{ice}}{\rho_{br}} S(\xi = 0, t)}{4\pi^2 \chi^2 \bar{D} - i2\pi\chi (br_j^\downarrow + \phi v_m(t))} \quad (23)$$

318

319 Taking the inverse Fourier transform of Equation 23 gives:

320

$$S(\xi, t) = \int_{-\infty}^{\infty} \left[\frac{v_m(t) \frac{\rho_{ice}}{\rho_{br}} S(\xi = 0, t)}{4\pi^2 \chi^2 \bar{D} - i2\pi\chi (br_j^\downarrow + \phi v_m(t))} \right] \exp(i2\pi\chi\xi) d\chi \quad (24)$$

322

$$= \frac{v_m(t) \frac{\rho_{ice}}{\rho_{br}} S(\xi = 0, t)}{(br_j^\downarrow + \phi v_m(t))} \left[\pm 1 \mp \exp\left(\frac{-\pi\xi (br_j^\downarrow + \phi v_m(t))}{\bar{D}}\right) \right] \quad (25)$$

324

325 Throughout this work we seek constitutive equations that relate the amount of salt entrained in
 326 forming ice to depth and local thermal gradient. Using the relationships of Equations 10 & 14, the
 327 definition of $\xi = z - z_m(t)$, and assuming in the active mushy layer near the ice-ocean interface,
 328 where reactive transport is possible, $z \sim z_m(t)$, we can rewrite Equation 25 in two forms:

329

$$S_{tot}(z_m) \propto \frac{1}{z_m} [1 - \exp(-z_m)] \quad (26)$$

331

$$S_{tot}\left(\frac{\partial T}{\partial z}\right) \propto \frac{\frac{\partial T}{\partial z}}{1 + \frac{\partial T}{\partial z}} \left[1 - \exp\left(-1/\frac{\partial T}{\partial z}\right) \right] \quad (27)$$

333

334 where the first term on the right-hand side of each equation is a diffusion term which dominates at
 335 later times (deeper depths, lower thermal gradients) and the second term is an advection-reaction
 336 term which dominates at early times (shallower depths, larger thermal gradients). Together,
 337 Equations 26 & 27 provide the functional forms for the constitutive equations produced throughout
 338 the remainder of the text.

339

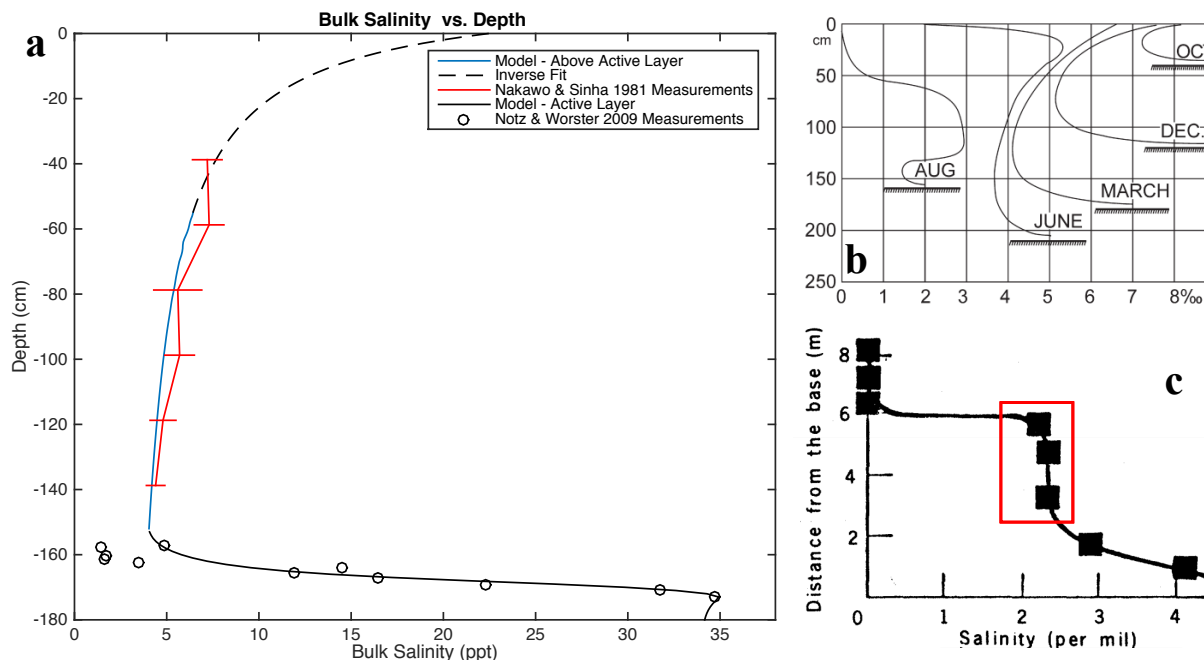
340 **3. Results**

341 3.1 Salt Entrainment on Earth

342

343 Two types of ice present on Earth provide the best end-member analogs for Europa's ice
 344 shell: sea ice and marine ice. Here, sea ice refers to frozen seawater at the ocean's surface, while
 345 marine ice is seawater-derived ice which has accreted onto the basal surface of meteoric ice shelves
 346 (e.g. [Zotikov *et al.*, 1980]). While both ices form via the directional solidification of seawater, and
 347 thus undergo the same dynamics during their formation, they form under different thermal regimes,
 348 resulting in unique compositional and physical structure. Sea ice provides the upper limit of
 349 impurity entrainment and an ideal analog for ice formed along steep thermal gradients near
 350 Europa's surface, as its formation is driven by rapid heat loss to the cold polar atmosphere.
 351 Fortunately, there exists nigh on a century's worth of observations and quantitative measurements
 352 regarding vertical heterogeneities in the thermal, chemical, and microstructural properties of sea
 ice [Malmgren and Institut, 1927]. With the proximity of the 100 K surface, a young, thin European

353 ice shell (tens to hundreds of meters thick) as well as any newly emplaced shallow liquid water
 354 features within the contemporary ice shell will experience similarly high thermal gradients,
 355 suggesting high impurity uptake akin to that of sea ice. We have previously modeled the annual
 356 growth of sea ice to study its thermochemical evolution and ability to record variations in ocean
 357 characteristics through the reproduction of ice core properties [Buffo *et al.*, 2018]. This model was
 358 adapted to actively track the advancing ice-ocean interface and accommodate potentially diverse
 359 ocean chemistries. In Figure 2, we present model results for sea ice and compare these to empirical
 360 measurements of depth dependent sea ice bulk salinity [M Nakawo and Sinha, 1981; Notz and
 361 Worster, 2009]. Actively tracking the evolution of the ice-ocean interface and simulating small-
 362 scale solute transport within the porous ice produces bulk salinity profiles that agree well with
 363 observations. We achieve salinity profiles that exhibit the characteristic ‘c-shape’ typical of first-
 364 year sea ice, represented by the ‘MARCH’ profile of Figure 2b [Malmgren and Institut, 1927],
 365 and reproduce the bulk salinity values observed in the field. Based on the constitutive relationship
 366 between depth and bulk salinity (Eq. 10), we use an inverse fit to the simulated values to extend
 367 the profile to the upper portion of the ice where extreme temperature gradients affect numerical
 368 stability when using a Neumann boundary condition. Thus, our model captures the physical
 369 processes that occur during ice formation in high thermal gradient environments, which will
 370 govern the formation of ice near Europa’s surface.
 371



372
 373 **Figure 2: Salinity profiles within observed and modeled marine and sea ice. a)** Modeled (blue and black solid
 374 lines), empirical (red line [M Nakawo and Sinha, 1981] and black circles [Notz and Worster, 2009]), and interpolated
 375 (black dashed line) bulk salinity profiles of sea ice. The numerical model assumes a preexisting 50 cm thick layer of
 376 sea ice in conductive equilibrium (linear temperature profile) with an atmospheric temperature of 250K and an ocean
 377 temperature of 271.5K. A conductive heat flux is maintained throughout the simulation at the upper boundary. The
 378 model was run for 1.5×10^7 sec (~ 174 days, a typical sea ice annual cycle) with a time step of 100 sec. The dashed line
 379 is the product of a Levenberg-Marquardt algorithm fit to the function $S(z) = a + b/(c-z)$, where S is bulk salinity, z is
 380 depth, and a , b , and c are constants, applied to the modeled bulk salinities above the active layer (blue solid line).
 381 While all of the bulk salinity values (blue and black solid lines) are a byproduct of the same model simulation, values
 382 in the active layer (black solid line) are excluded from the Levenberg-Marquardt fit (black dashed line) as the
 383 constitutive equations (Table 3) are derived assuming an infinitesimally thin mushy layer. **b)** Typical first-year sea ice

384 salinity profiles have a characteristic ‘c’ shape where the bulk salinity evolves over the season due to material transport
 385 and ice growth (from [Malmgren and Institut, 1927]). c) Bulk salinity measurements from the bottom 8 m of an ice
 386 core extracted from the Ross Ice Shelf by [Zotikov et al., 1980]. The bottom 6 m is accreted marine ice, with the
 387 ‘asymptotic region’ outlined in red approaching diffusive equilibrium during ice formation.

388 Conversely, as thermal gradients decrease, ice composition approaches an asymptotic
 389 lower limit governed by the critical porosity of the active layer when it is in diffusive equilibrium
 390 with the underlying ocean. Here, critical porosity is analogous to a percolation threshold, where
 391 regions with porosities below this limit are no longer hydraulically connected to the surrounding
 392 pore network and any remaining salt is trapped in discrete brine pockets. Much of Europa’s deeper
 393 ice shell, below about 1 km, will have formed under these conditions. A similar environment exists
 394 at the base of deep ice on Earth, called marine ice [Zotikov et al., 1980]. This unique, and less
 395 studied, variety of ocean-derived ice forms on the basal surface of terrestrial ice shelves due to
 396 much lower thermal gradients than typical open ocean sea ice (e.g. ~10 K/m for surficial sea ice;
 397 ~0.08 K/m for marine ice [Zotikov et al., 1980]) leading to greatly reduced growth rates (~2 cm/yr
 398 [Zotikov et al., 1980]). While the thermal gradients present in the marine ice system (~0.08 K/m)
 399 exceed the upper estimates for a thin (5-10 km) European ice shell (~0.02 K/m) [McKinnon, 1999;
 400 Mitri and Showman, 2005], they represent the best terrestrial analog of basally accreting ice in this
 401 thermal regime, and it can be shown that impurity entrainment has already approached its lower
 402 limit – characterized by asymptotic bulk salinity profiles (Figure 2c). Adopting a critical porosity
 403 of $\phi_c = 0.05$, based on observations of sea ice permeability [K Golden et al., 1998; K M Golden
 404 et al., 2007], and assuming an ocean salinity, $S_{oc} = 34 \text{ ppt}$, the theoretical lower limit for salt
 405 entrainment into terrestrial ice (diffusive equilibrium when impermeability is reached) is given by
 406 $S_{lim} = \phi_c S_{oc} = 1.70 \text{ ppt}$. The average bulk salinity of the ‘asymptotic region’ seen in Figure 2c
 407 is 2.32 ppt. Utilizing the constitutive equation for bulk salinity versus thermal gradient derived in
 408 the next section for terrestrial seawater in the diffusive regime ($dT/dz = 0.08 \text{ K/m}$), a bulk salinity
 409 of 1.95 ppt is predicted. The difference of 0.37 ppt between the observed and predicted bulk
 410 salinity values translates to a 16% error, attributed to small variations in unconstrained parameters,
 411 such as critical porosity and permeability-porosity relationships (both of which can appreciably
 412 affect impurity entrainment rates [Buffo et al., 2018]). The efficiency of brine migration through
 413 the porous ice lattice and the threshold at which percolation is possible are poorly constrained [K
 414 Golden et al., 1998; K M Golden et al., 2007; Wells et al., 2011] but govern the dynamics of
 415 multiphase flow, brine retention in the ice, and ultimately ice composition. At the ice-ocean/brine
 416 interface, reduced permeability or a larger critical porosity would lead to more salt being entrained
 417 in the ice. Alternately, enhanced permeability or a smaller critical porosity would result in less salt
 418 entrainment. Nevertheless, our model closely reproduces observations of sea ice, and the same
 419 multiphase reactive transport physics applied in low-thermal gradient conditions match
 420 observations of marine ice composition, which capture broadly the two thermochemical regimes
 421 that ice on Europa is expected to occupy.

422

423 3.2 The Role of Thermal Gradients and Ocean Chemistry

424 Aside from the different surface temperature (<110 K vs ~250 K), gravity (1.32 vs 9.81
 425 m/s^2) and potential compositional characteristics between Europa and Earth, one of the largest
 426 differences is sheer scale of the ice. While the majority of sea ice exhibits a maximum thickness
 427 of <10 m [Kurtz and Markus, 2012; Laxon et al., 2013] (ice drafts have been known to exceed 25
 428 m and reach up to 47 m beneath pressure ridges [Davis and Wadhams, 1995; Lyon, 1961]) and
 429 marine ice accretion occurs at depths <1.5 km [Craven et al., 2009; Galton - Fenzi et al., 2012;

430 *Zotikov et al.*, 1980], Europa's ice shell is likely 10-30 km thick [*Billings and Kattenhorn*, 2005;
431 *F Nimmo et al.*, 2003; *Tobie et al.*, 2003]. It is important to note, however, that despite differences
432 in ice thickness, all ice-ocean interfaces will remain at or near their pressure melting point, which
433 for a 1.5 km thick terrestrial ice shelf is comparable to an ~11.1 km thick European ice shell.
434 Modeling the entire ice shell thickness and lifespan at the resolution needed to capture the reactive
435 transport dynamics occurring near the ice-ocean/brine interface is computationally intractable. To
436 overcome these difficulties, we modified our model [*Buffo et al.*, 2018] such that it actively tracks
437 only the permeable or 'active' region of the ice shell, determined by the critical porosity where
438 fluid flow ceases [*K Golden et al.*, 1998; *K M Golden et al.*, 2007]. In the top-down solidification
439 scenarios modeled, when the fluid fraction of a discretized layer drops below the critical porosity
440 it is removed from the active domain and its properties are cataloged, along with all the cells above
441 it, and an equal number of replacement layers are added to the bottom of the domain with ambient
442 ocean/brine characteristics ($T_{oc}, S_{oc}, \rho_{sw}$). Model runs are initiated with the domain completely
443 filled by one of the ocean chemistries investigated at a temperature just above its freezing point
444 (Supplementary Section S1). The top boundary is governed by a Neumann boundary condition
445 with a no-flux condition set for salt and it is assumed that the overlying ice is in conductive thermal
446 equilibrium [*McKinnon*, 1999] (i.e. $dT/dz = (T_{oc} - T_s)/H$). The bottom boundary is governed
447 by a Dirichlet boundary condition and is simulated as being in contact with an infinite ambient
448 ocean/brine reservoir ($T_{oc}, S_{oc}, \rho_{sw}$) (for additional information on code functionality see [*Buffo et*
449 *al.*, 2018]). To construct the full ice shell from discrete model runs, several simulations at various
450 depths (solidification front locations) run in parallel, and the results are combined to produce the
451 constitutive relationships that relate ice composition to its thermochemical environment at the time
452 of formation. It is important to note that the top-down unidirectional solidification of Europa's ice
453 shell from a quiescent ocean is likely a simplification as the aqueous differentiation of its juvenile
454 planetesimal was likely a tumultuous and complex process [*Kargel et al.*, 2000]. This formation
455 scenario was selected as it mirrors the formation of sea and marine ice, the only benchmarks
456 available for the formation of ocean-derived ices. Moreover, the functional forms of the
457 constitutive equations are derived under such conditions, requiring simulations of this type to
458 derive the bulk salinity-thermal gradient relationships paramount to the remainder of the
459 manuscript (e.g. basal fracture and perched lens solidification).

460 Composition of the ocean is critical to ice formation because of the relationship between
461 the salinity of water and its freezing point. The conductive nature of Europa's ocean [*Khurana et*
462 *al.*, 1998; *Kivelson et al.*, 2000], as well as spectrographic measurements [*McCord et al.*, 1999],
463 suggests the presence of dissolved salts, but nearly all of its intrinsic properties (thickness,
464 composition, structure) remain poorly constrained. Potential European ocean chemistries have been
465 explored in a number of studies [*Vance et al.*, 2016; *M Yu Zolotov and Kargel*, 2009; *Mikhail Y*
466 *Zolotov and Shock*, 2001]. Here we implement the chemistry proposed by [*Mikhail Y Zolotov and*
467 *Shock*, 2001], who assumed that Europa's ocean formed during its differentiation via partial
468 aqueous extraction from bulk rock with the composition of CV carbonaceous chondrites (Table
469 2). Alternate formation materials (e.g. CI chondrites [*M Yu Zolotov and Kargel*, 2009]) will alter
470 the predicted ionic composition of the ocean, and variable molecular diffusivities, atomic masses,
471 and v'ant Hoff factors may affect impurity entrainment rates in associated ocean-derived ices. For
472 comparison, we also considered an ocean composition identical to terrestrial seawater (Table 2).
473 Well-known liquidus curves exist for terrestrial seawater [*Commission*, 2010]. However, the
474 freezing behavior of potentially more exotic European ocean compositions is comparatively less
475 well known, so we constructed a new software package, Liquidus 1.0, to derive quadratic liquidus

476 curves for any chemistry supported by the equilibrium chemistry package FREZCHEM 6.2, which
 477 includes a wide range of material properties for the expected non-ice components of brines
 478 (Supplementary Section S1).

479

Species	Terrestrial Seawater (mol/kg)	European Ocean (mol/kg)
Na ⁺	4.69 x 10 ⁻¹	4.91 x 10 ⁻²
K ⁺	1.02 x 10 ⁻²	1.96 x 10 ⁻³
Ca ²⁺	1.03 x 10 ⁻²	9.64 x 10 ⁻³
Mg ²⁺	5.28 x 10 ⁻²	6.27 x 10 ⁻²
Cl ⁻	5.46 x 10 ⁻¹	2.09 x 10 ⁻²
SO ₄ ²⁻	2.82 x 10 ⁻²	8.74 x 10 ⁻²
Total Salt (ppt)	34	12.3

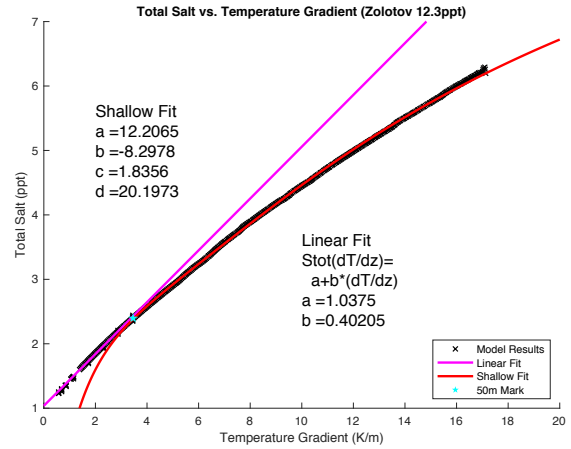
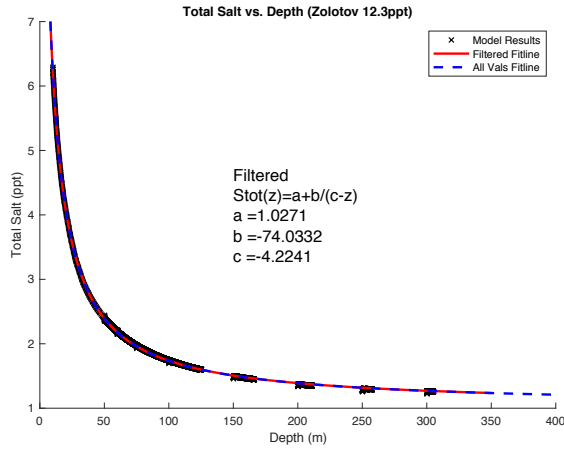
480 **Table 2 – Ocean compositions.** List of ion species and relative abundances for terrestrial seawater [Dickson and
 481 Goyet, 1994] and the proposed European ocean chemistry of [Mikhail Y Zolotov and Shock, 2001].

482

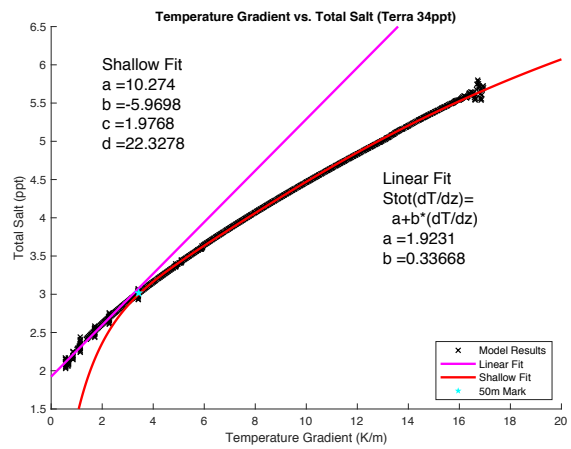
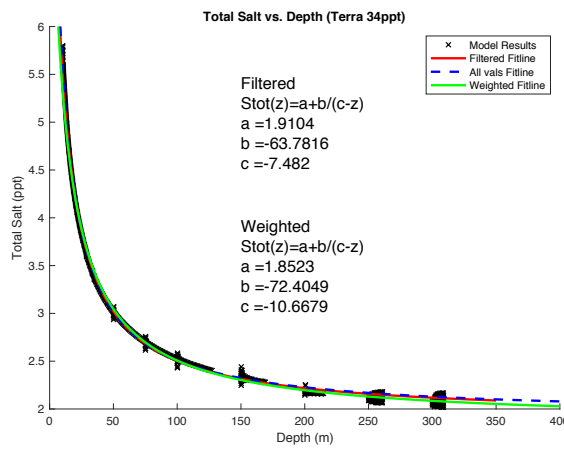
483 We forego simulating the possible precipitation of hydrated salts (e.g. mirabilite ($Na_2SO_4 \cdot$
 484 $10H_2O$) [Butler et al., 2016], epsomite ($MgSO_4 \cdot 7H_2O$), meridianiite ($MgSO_4 \cdot 11H_2O$)
 485 [McCarthy et al., 2011; McCarthy et al., 2007]) for two reasons. First, implementing reactive
 486 transport modeling to simulate the evolution of ice-ocean worlds is a relatively novel approach,
 487 thus it is logical to begin with the simpler ice-brine binary system (as opposed to the ice-brine-
 488 hydrate ternary system), to both validate the approach and obtain a first order understanding of
 489 how salts are entrained in planetary ices. Second, the low thermal gradients experienced
 490 throughout much of the shell will facilitate slow ice growth, allowing for the dissipation of salt
 491 from high salinity regions via both convection and diffusion, preventing saturation and
 492 precipitation. Future work investigating ternary systems could reveal additional bulk salinity
 493 profile structure in the shallow ice shell brought about by the precipitation of such hydrated salts.

494 We simulated Europa's ice shell growth at eight discrete ice thicknesses (10 m, 50 m, 75
 495 m, 100 m, 150 m, 200 m, 250 m, and 300 m), for four different hypothetical ocean compositions
 496 (European Ocean 12.3 ppt/100 ppt/282 ppt and Terrestrial Seawater 34 ppt). By the time the ice
 497 shell reaches 300 m in thickness the thermal gradient at the ice-ocean interface is shallow enough
 498 that the bulk salinity curve becomes asymptotic and variations in the salt entrainment rate will be
 499 minimal at all greater depths. This asymptotic lower limit is set by the ocean composition and
 500 critical porosity ($S_{lim} = \phi_c S_{oc}$). Simulations of larger ice thicknesses (>300 m) were therefore
 501 excluded, given the predicted ice composition below 300 m would vary by <1 ppt (see the first
 502 row of Table 3 and the following paragraph). European ocean concentrations were selected to bound
 503 the best estimates available from theory and observation: the most comprehensive estimate
 504 provided from theoretical calculations is 12.3 ppt [Mikhail Y Zolotov and Shock, 2001], while the
 505 saturation point of the same fluid would reach an ocean salinity of 282 ppt, and the upper limit
 506 based on the Galileo magnetometer data estimates a salinity of 100 ppt [Hand and Chyba, 2007].
 507 The results for all ocean compositions can be seen in Figure 3 and Supplementary Figure S4. The
 508 results are depth-dependent and thermal gradient-dependent bulk salinity profiles, which are then
 509 interpolated using a Levenberg-Marquardt algorithm fit to the constitutive equations, the explicit
 510 form of which, including the coefficients needed to accommodate stretches and translations, are
 511 shown in Table 3.

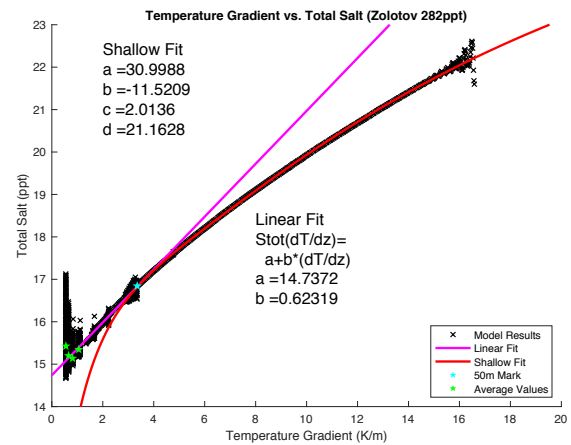
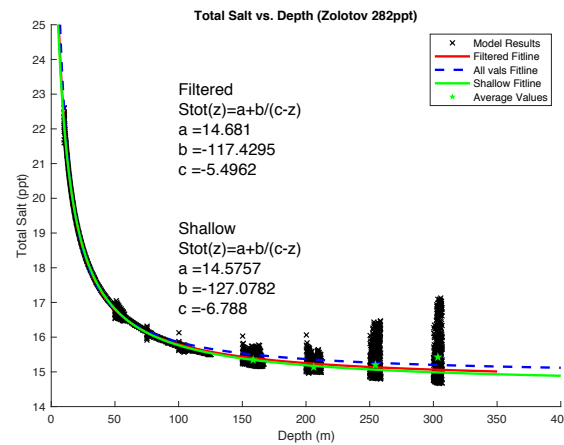
512



513



514



515

Figure 3: Simulations of depth dependent and thermal gradient dependent bulk salinity for three different ocean chemistries (100 ppt simulation is presented in Figure S4) Relationships are fit by the constitutive equations of Table 3. Left Column, Model results [black exes] (numerical dispersion at the onset of each run has been removed) and original (all values), filtered (numerical dispersion at run onset removed), weighted (where applicable – weighted by data density), and shallow (where applicable – fitting model results from 10-200 m runs) fit lines [blue dashed line, red line, and green lines, respectively]. Right Column, Simulated results [black exes] as well as linear and ‘Shallow’ (See Table 3) fit lines [pink and red lines, respectively]. Green stars represent average bulk salinity for an entire run at a given depth – highlighting that the majority of the simulated data lies near the fit lines, even when scatter is present. Blue stars identify the thermal gradient associated with a 50 m depth within an equilibrated conductive ice shell, which is the transition point between the diffusive and advective-reactive regimes.

Constitutive Equation	a	b	c	d
$S_{tot}(z) = a + \frac{b}{(c-z)}$	a _{12.3} =1.0271 a ₁₀₀ =5.38 a ₂₈₂ =14.681 a ₃₄ =1.8523	b _{12.3} =-74.0332 b ₁₀₀ =-135.096 b ₂₈₂ =-117.429 b ₃₄ =-72.4049	c _{12.3} =-4.2241 c ₁₀₀ =-8.2515 c ₂₈₂ =-5.4962 c ₃₄ =-10.6679	
$S_{tot}\left(\frac{\partial T}{\partial z}\right) = a + b\frac{\partial T}{\partial z}$	a _{12.3} =1.0375 a ₁₀₀ =5.4145 a ₂₈₂ =14.737 a ₃₄ =1.9231	b _{12.3} =0.40205 b ₁₀₀ =0.69992 b ₂₈₂ =0.62319 b ₃₄ =0.33668		
(Shallow Fit Line) $S_{tot}\left(\frac{\partial T}{\partial z}\right) = a + \frac{b\left(\frac{\partial T}{\partial z} + c\right)}{1 + \frac{\partial T}{\partial z}} \left[1 - \exp\left(\frac{-d}{\partial T/\partial z}\right)\right]$	a _{12.3} =12.21 a ₁₀₀ =22.19 a ₂₈₂ =31.00 a ₃₄ =10.27	b _{12.3} =-8.30 b ₁₀₀ =-11.98 b ₂₈₂ =-11.52 b ₃₄ =-5.97	c _{12.3} =1.836 c ₁₀₀ =1.942 c ₂₈₂ =2.014 c ₃₄ =1.977	d _{12.3} =20.20 d ₁₀₀ =21.91 d ₂₈₂ =21.16 d ₃₄ =22.33

Table 3: Constitutive Equations. The reactive transport model results are fit by constitutive equations relating bulk salinity to shell depth and temperature gradient for each of the ocean compositions, column 1, and their associated coefficients, a-d. Subscripts 12.3, 100, 282, and 34 refer to European ocean compositions with concentrations of 12.3 ppt, 100 ppt, 282 ppt, and terrestrial seawater with a concentration of 34 ppt, respectively. These equations provide a parameterization of Europa's ice shell composition's dependence on the local thermal environment at the time of ice formation, which can be utilized to provide efficient first order estimates of the properties of ice formed in a variety of chemical and thermal environments without the need for explicit simulation.

The translation of the model from the Earth system to Europa hinges on the observation that as thermal gradients near the ice-ocean/brine interface decrease ice bulk salinity asymptotically approaches a lower limit governed by molecular diffusion in the pore fluid (Figure 2c). The result of this is twofold. First, the ice shell will experience ice-ocean interface thermal gradients below those found on Earth during much of its formation. This suggests a relatively homogeneous ice layer (formed in the asymptotic regime) underlying a thin (~1 km), compositionally distinct surficial layer (formed under steep thermal gradients). This stratification would produce variations in the thermochemical and mechanical properties of these layers, potentially introducing a boundary along which rheological transitions (e.g. brittle lid vs. ductile mantle) and transport regimes (conduction vs. convection) may be promoted. Second, the lower portion of the contemporary ice shell is believed to be ductile enough to undergo solid state convection [Barr and McKinnon, 2007; Han and Showman, 2005; McKinnon, 1999; Tobie et al., 2003], providing a mechanism that would mix this region of the shell, homogenizing it chemically and flattening its thermal profile (consider the analogous geothermal profile). A convective thermal profile in this ductile region suggests an ice-ocean interface subject to very low thermal gradients [Mitri and Showman, 2005], implying that accreted ice salinities would be at or near their lower limit, irrespective of ice thickness. Thus, the ductile region of the contemporary ice shell should have a bulk composition at or near the lower limit set by the critical porosity. Such a compositional profile varies negligibly from those predicted by the unidirectional solidification scenarios we simulate here (below 1 km predicted salinities vary by <150 ppm from the theoretical lower limit). Any heterogeneities in impurity entrainment would require associated ice-ocean heat flux variations (e.g., ocean driven heating of the ice shell [Soderlund et al., 2014], thermochemical diapirism [R T Pappalardo and Barr, 2004], spatiotemporal variations in basal heat flux due to downwelling cold ice and/or the evolution of tidal heating within the ice shell [Tobie et al., 2003]) with amplitudes large enough to appreciably affect entrainment rate. Notably, this implies that for much of the ice shell it is not the thermal regime of the ice but rather its critical porosity and permeability which will determine ice composition.

551 In general, the bulk salinity profiles and their corresponding relationships to depth within
 552 the ice shell and local temperature gradients are well-represented by our derived constitutive
 553 equations, suggesting that their functional forms (Eq. 26 & 27) capture much of the reactive
 554 transport physics that govern how ice forms in the presence of dissolved materials, and the
 555 movement of this material via advection and diffusion while the ice is still permeable. The division
 556 of impurity entrainment rate into two distinct thermal regimes, diffusive (low) and advective-
 557 reactive (high), is well accommodated and justified by the terrestrial benchmarks above. While
 558 there exist uncertainties in the limit of extreme thermal gradients ($\gg 20 K/m$) and large salinities
 559 (e.g. scatter observed for the 282 ppt ocean at low thermal gradients, a consequence of salinity's
 560 increased sensitivity to changes in porosity at high ocean concentrations [Supplementary Section
 561 S5]), the high thermal conductivity of ice relative to water quickly diffuses such thermal
 562 anomalies, and the results demonstrate that, as expected, the bulk salinity in the ice approaches the
 563 diffusive equilibrium limit under low thermal gradients. Thus, as perhaps the first quantitative
 564 estimate of impurity content, the constitutive equations derived here allow us to investigate the
 565 properties and evolution of Europa's ice shell and hydrological features contained therein.

566

567 3.3 The Evolution of Europa's Ice Shell

568 3.3.1 Total Salt

569 The constitutive equations derived above can be used to estimate the total salt content of
 570 Europa's ice shell prior to the onset of solid-state convection, producing an upper limit on the total
 571 impurity load of the ice shell. For these calculations, we assume a 25 km thick ice shell with an
 572 inner radius of 1,535 km and an outer radius of 1,560 km. The total salt content for a given ocean
 573 composition can be calculated by integrating the constitutive equation over the volume of the ice
 574 shell given the coefficients in Table 3. For an ice shell with inner radius R_1 and outer radius R_2 ,

$$575 \quad \text{Total Salt in Shell} = \frac{\rho_{ice}}{1000} \int_V S_{tot}(z) dV \quad (28)$$

576

577 where ρ_{ice} is the density of ice, V is the volume of the ice shell, and $S_{tot}(z)$ is the constitutive
 578 equation relating bulk salinity and depth (Table 3). Rewriting z in terms of the spherical coordinate
 579 r , gives:

580

$$581 \quad \text{Total Salt in Shell} = \frac{\rho_{ice}}{1000} \int_{R_1}^{R_2} \int_0^{2\pi} \int_0^{\pi} \left[a + \frac{b}{(c - (R_2 - r))} \right] r^2 \sin \varphi \, dr \, d\theta \, d\varphi \quad (29)$$

582

583 where a , b , and c are coefficients from the ocean/brine specific constitutive equation and (r, θ, φ)
 584 represent a spherical coordinate system.

585 The total volume of the 25 km thick European ice shell is $\sim 7.5235 \times 10^{17} \text{ m}^3$, while the
 586 approximate collective volume of Earth's oceans is $\sim 1.332 \times 10^{18} \text{ m}^3$ [Charette and Smith, 2010].
 587 For the European ocean composition (Table 2), with concentrations of 12.3 ppt, 100 ppt, and 282
 588 ppt the total salt entrained in a 25 km shell is $7.2894 \times 10^{17} \text{ kg}$, $3.6633 \times 10^{18} \text{ kg}$, and 1.0189×10^{19}
 589 kg, respectively. This corresponds to average ice shell salinities (total salt/ice shell mass) of 1.0565
 590 ppt, 5.3099 ppt, and 14.769 ppt, respectively. For a terrestrial ocean composition with a
 591 concentration of 34 ppt the total salt entrained in a 25 km shell is $1.2978 \times 10^{18} \text{ kg}$, corresponding

592 to an average ice shell salinity of 1.8811 ppt. For comparison, Earth's oceans contain $\sim 4.5288 \times$
 593 10^{19} kg of salt.

594 Directly related to the composition and bulk salinity of the ice is its density. Crucial in
 595 driving any potential solid-state convection on Europa, compositional buoyancy may either help
 596 or hinder large scale, thermally driven convective overturn in the ice shell. Horizontal density
 597 gradients have also been proposed as a driver of putatively observed subduction/subsumption on
 598 Europa's surface [Johnson *et al.*, 2017b; Kattenhorn, 2018]. Mirroring the profiles of bulk salinity,
 599 there exists a rapid and asymptotic decrease in ice density with depth for all ocean chemistries
 600 (Supplementary Figure S5), and subsequently throughout much of the shell the density is nearly
 601 homogeneous (e.g. for a 100 ppt European ocean chemistry $\rho_{500m}=922.54 \text{ kg/m}^3$ and
 602 $\rho_{25km}=922.25 \text{ kg/m}^3$). Our results demonstrate that, apart from a geophysically thin surface layer,
 603 significant variations in density with depth are unlikely to form as the ice shell freezes out. The
 604 maximum salt content predicted in the near surface is ~ 36 ppt (or $\sim 3.6\%$), calculated by extending
 605 the constitutive equation relating bulk salinity and shell depth for the 282 ppt ocean to the surface
 606 ($z = 0$). The same calculation for the 100 ppt, 34 ppt, and 12.3 ppt oceans results in near surface
 607 salt contents of ~ 22 ppt, ~ 9 ppt, and ~ 19 ppt (or $\sim 2.2\%$, $\sim 0.9\%$, and $\sim 1.9\%$), respectively. A
 608 number of these values are greater than, or close to, the 2% salt content needed to drive the
 609 subduction of certain laterally compositionally heterogeneous slabs calculated by [Johnson *et al.*,
 610 2017a]. However, the physical, thermal, and chemical characteristics of the ice shell likely act in
 611 concert to control Europa's dynamics, as the material properties of ice are structurally, thermally,
 612 and chemically dependent (Supplementary Section S2). The expected salinity profile, along with
 613 the total impurity load, provides context on the nature of liquid and solid phases within the ice
 614 shell. Combined with thermal variations due to convection, tidal heating, or heat transfer from the
 615 ocean [Howell and Pappalardo, 2018; Mitri and Showman, 2005] and variations in physical
 616 properties such as porosity and viscosity [Barr and McKinnon, 2007; Johnson *et al.*, 2017a], more
 617 explicit constraints on the thermophysical formation of many of Europa's surface features are thus
 618 possible.

619

620 3.3.2 Basal Fractures

621 The fundamental processes that occur during the freezing of ice are not only applicable to
 622 the ocean, but to any water within the ice shell. We adapted our approach to accommodate the
 623 geometry of simple basal fractures (Supplementary Section S3), to investigate the composition of
 624 fractures upon re-freezing. Akin to the basal fractures of terrestrial ice shelves, fractures at the ice-
 625 ocean or other ice-liquid interface of Europa could either locally stabilize or destabilize the ice
 626 shell; they have the potential to suture the shell back together with newly frozen oceanic material
 627 [Khazendar *et al.*, 2009], or to propagate further, potentially penetrating to the surface [Bassis and
 628 Walker, 2011]. Such fractures appear within Europa's chaos terrain [Walker and Schmidt, 2015],
 629 a potential indicator of near-surface water reservoirs [Schmidt *et al.*, 2011] and a potential pathway
 630 for shallow water to make it to the surface in the form of plumes [Sparks *et al.*, 2017] (See Figure
 631 1a).

632 We modeled basal fractures at both Europa's ice-ocean interface and a hypothetical ice-
 633 lens interface (Figure 4). The fractures are filled with fluid from the underlying reservoir (ocean
 634 or lens) and the fluid is assumed to remain well mixed during the simulations since the advective
 635 timescale for rejected brine with a density 1 kg m^{-3} greater than the ambient fluid through a 25 km
 636 fracture is <1 day (equating gravitational and viscous drag forces for a parcel of brine near the
 637 crack tip of width $\mathcal{O}(1)$, $v \sim \Delta\rho g/\eta$). Due to the high aspect ratio of the basal fractures (penetration

638 depth/basal width) we modeled them as solidifying horizontally inward, akin to how terrestrial
 639 magmatic dikes form, forced by the conductive profile of the ice shell into which the fracture is
 640 emplaced. The injection of water into the ice shell produces regions of very high thermal gradients
 641 between the relatively warmer water and cold ice. As a result, fractures refreeze to form ice wedges
 642 with chemically gradated composition, due to the amplified solidification rates at the fracture's
 643 edges and tip. While these simulations do not completely capture all of the inherently two-
 644 dimensional structure of the fracture (especially near the crack tip) these results currently provide
 645 the most realistic evaluation of basal fracture physicochemical evolution. The results suggest that
 646 basal fractures are geologically short-lived, at least in the upper shell, due to their high aspect ratios
 647 and rapid heat loss to the surrounding ice. At depth their lifetime may be extended by deformation
 648 processes brought about by tidal forces [*Francis Nimmo and Gaidos, 2002*] or the presence of a
 649 warmer ductile ice layer [*Barr and McKinnon, 2007; Tobie et al., 2003*]. While it is unlikely that
 650 fractures in the shallow shell contain liquid water for long, we show that the rapid injection and
 651 refreezing of saline fluid within a colder ice shell produces local chemical heterogeneities along
 652 the fracture walls that could preserve the fracture. Two important implications arise: the high
 653 salinity regions along the fracture walls produce a gradient in mechanical properties, potentially
 654 weakening the center of the fracture or concentrating stress here, while at the same time these
 655 regions could be more easily melted during reactivation of the fracture even in the absence of water
 656 from the ocean. Both of these provide mechanisms by which features can remain active even once
 657 they refreeze.

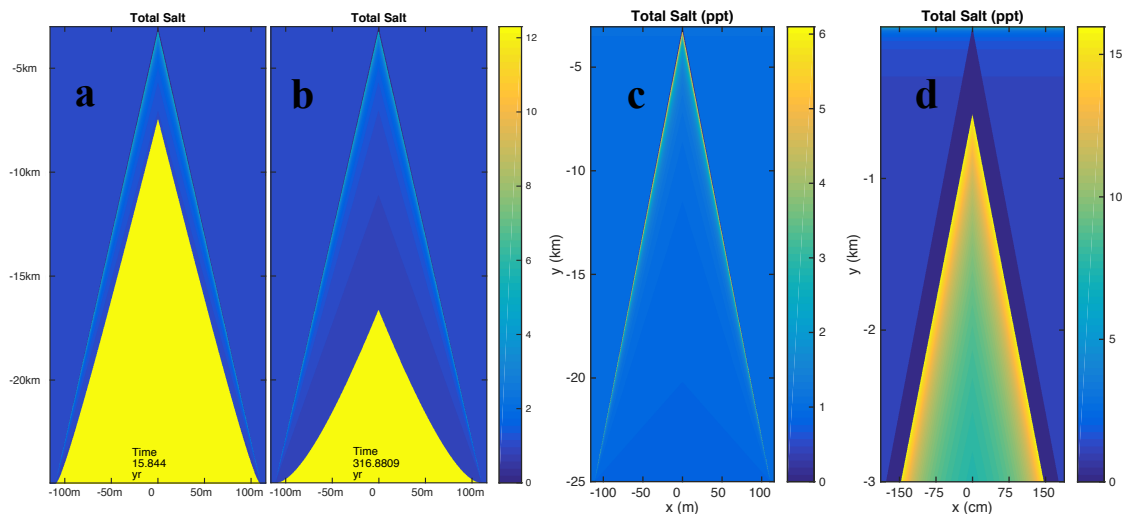


Figure 4: Basal ice fractures refreeze to produce a gradient in salinity. Temporal evolution of a hypothetical basal fracture, **a-b** (Supplementary Figures S7-8 and Sections S3-4), shows that rapid refreezing occurs, down to 5km within 15 years if the fracture can be held open over this timeframe. Profiles for deep fractures from the ice-ocean interface, **c** (due to 2 MPa stress in a 25 km shell; Depth – 21.925 km, Width – 220.9 m), and fractures from shallow lens interfaces, **d** (due to 2 MPa stress in a 3 km lid, Depth – 2.922 km, Width – 3.53 m), show similar patterns of high salt content along the fracture wall and toward the tip, and lower salinity toward the interior and base. These results show that gradients in mechanical properties are likely toward the surface where tidally modulated activity is more likely. For fractures from the ocean, the majority of the ice formed in the interior of the fracture, however, will have a salinity that is nearly indistinguishable from the bulk Europa ice. This suggests that fractures are likely to be regions of local discontinuities in ice shell properties, and potentially regions of weakness within the ice shell created by interfaces between salt and ice grains.

660 3.3.3 Brines within the Ice

661 Knowing the composition of the ice provides the chance to evaluate the formation,
 662 evolution, and longevity of water or brine systems within Europa's ice shell. For example, shallow
 663 lenses of liquid water are suggested to form *in situ* via melting of the ice shell [Schmidt *et al.*,
 664 2011] (Figure 1a) or by injection through diking processes [Manga and Michaut, 2017; Michaut
 665 and Manga, 2014]. For such a lens, assuming the ice shell derived from a 34 ppt terrestrial ocean
 666 chemistry, letting the diffusive limit govern ice bulk salinity as shown above ($S_{lim} = \phi_c S_{oc}$) and
 667 tracking the evolving lens salinity, upon top down refreeze a 2 km thick lens located 1 km beneath
 668 a 100 K surface will produce ice compositions ranging from 0.0946 to 14.10 ppt. Additionally,
 669 upon complete refreeze, impurity rejection leads to the precipitation of an approximately 2.23 m
 670 layer of pure salt, assuming a saturation limit of 282 ppt (Figure 5). Thus, impurity entrainment
 671 and rejection during freezing produce compositional heterogeneities within the ice shell and
 672 introduce a concentration process capable of producing layers within the shell that have highly
 673 distinct mechanical, thermal, and dielectric properties. The ability to predict compositional
 674 variations around putative hydrological features in Europa's shell will both constrain how these
 675 features form and inform spacecraft observations [Blankenship *et al.*, 2009; Kalousová *et al.*,
 676 2017].

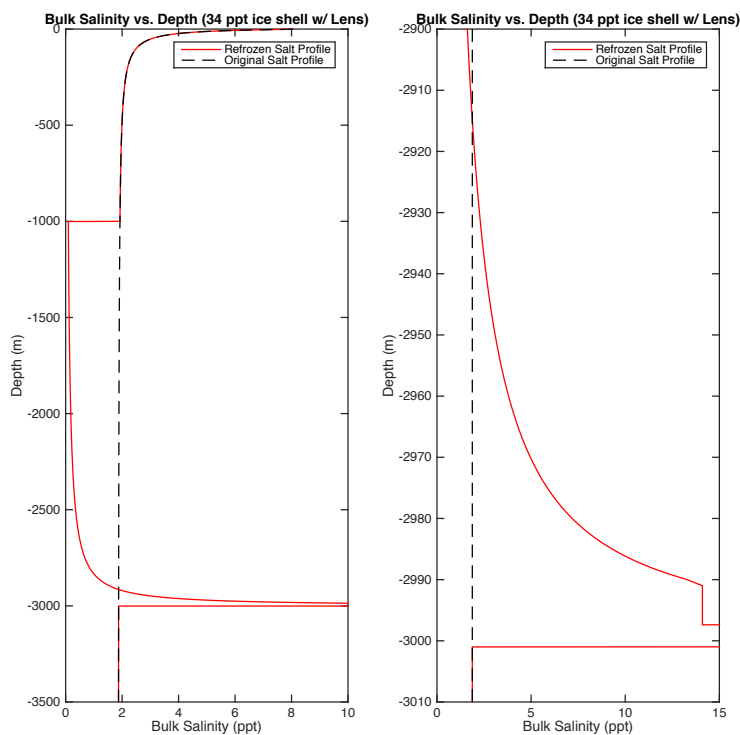


Figure 5: Bulk salinity profile of a perched water lens upon re-solidification. Left) A 2 km thick lens is assumed to form via the *in situ* melting of a preexisting ice shell, whose original composition is given by the black dashed line. Initially the lens salinity is less than that of the original ocean, but upon top down solidification salt is concentrated in the remaining liquid phase, leading to an increase in ice bulk salinity [red line] near the base of the refrozen lens as well as ~ 2.23 m of precipitated salt on the lens floor (1000 ppt values excluded from plot). **Right)** A magnified view of ice bulk salinity near the bottom of the lens (2.90 – 3.01 km). The lens saturates (282 ppt) when the ice reaches 2991 m, resulting in salt precipitation (2997.77 – 3000 m). 677

678

679 **4. Discussion**

680 The impurity load and distribution of entrained ocean materials within Europa's ice shell
 681 impacts the evolution of the ice shell, Europa's geology, and interactions between the surface and
 682 the ocean. Salts affect the rheological properties of the ice, especially relative to pure water ice,
 683 which impacts its mechanical behavior [Durham *et al.*, 2010]. We explicitly quantify the overall
 684 impurity content of Europa's ice shell, suggesting an average composition (total salt/ice shell
 685 mass) of between 1.053 and 14.72 ppt of non-ice material (depending on ocean composition),

686 which can be included in more realistic models of the geophysical evolution of the ice shell. These
687 results also demonstrate regions of high material contrast within the ice shell that could promote
688 or extend geologic activity. Compositional heterogeneities can either aid or prevent buoyancy
689 driven convection in the ductile region of the ice shell, which is important for constraining the
690 rates of subduction and surface recycling [Johnson *et al.*, 2017b; Kattenhorn, 2018]. Determining
691 the lifetime of liquid water features within the ice shell is of profound importance in considering
692 whether such reservoirs could be putative habitats; relevant for both planetary exploration and
693 planetary protection. While our models suggest that shallow subsurface water in a conductive ice
694 shell is short lived, the warmer, isothermal regime of an ice shell undergoing convection may
695 provide an environment where hydrological features could persist for much longer. New
696 constraints on the average density and composition of the ice feeds forward into the putative
697 reductant-oxidant cycle associated with ocean-surface interaction [Vance *et al.*, 2016], by which
698 ice shell overturn delivers surface-generated oxidants and ice-shell derived chemical species as
699 potential energy sources to the ocean. Compositional profiles of the bulk ice shell and geologic
700 features effectively capture the thermal and physicochemical nature of the ice that can be observed
701 by Europa Clipper's remote sensing and radar instruments: the spatial distribution of impurities on
702 the surface and the dielectric properties of the ice and water within the shell carry with them an
703 accessible fingerprint of ice shell dynamics and the ocean below.

704

705 **Acknowledgments**

706 **General**

707 The authors thank Sven Simon (Georgia Institute of Technology) for helpful discussions regarding
708 the analytical solution of the modified Stefan Problem.

709

710 **Funding**

711 This study was supported by the NASA Earth and Space Science Fellowship, grant NNX16AP43H
712 S01 and NNX16AP43H S002. Britney Schmidt was additionally supported by the Europa Clipper
713 Mission. Resources supporting this work were provided by the NASA High-End Computing
714 (HEC) Program through the NASA Advanced Supercomputing (NAS) Division at Ames Research
715 Center.

716

717 **Author Contributions**

718 J. J. B. contributed in designing the research, constructing the multiphase reactive transport model,
719 carrying out the research, interpreting the results, and writing/reviewing the paper.

720 B. E. S. contributed in designing the research, interpreting the results, and writing/reviewing the
721 paper.

722 C. H. contributed in constructing the multiphase reactive transport model, interpreting the results,
723 and writing/reviewing the paper.

724 C. C. W. contributed in constructing the fracture mechanics model, interpreting results, and
725 writing/reviewing the paper.

726

727 **Competing Interests**

728 The authors declare no competing financial nor non-financial interests.

729

730 **Materials and Correspondence**

731 *Code Availability*

732 Liquidus 1.0 and its associated documentation can be found at:

733 <https://github.com/jbuffo/Liquidus-1.0>

734 SlushFund 2.0 and its associated documentation can be found at:

735 <https://github.com/jbuffo/SlushFund-2.0---Active-Interface-Tracking>

736

737 All correspondence and material requests should be made to Jacob J. Buffo at:

738 jacob.buffo@eas.gatech.edu

739

740 **References**

- 741 Barr, A. C., and W. B. McKinnon (2007), Convection in ice I shells and mantles with self-
742 consistent grain size, *Journal of Geophysical Research: Planets*, 112(E2).
- 743 Bassis, J., and C. Walker (2011), Upper and lower limits on the stability of calving glaciers from
744 the yield strength envelope of ice, *Proc. R. Soc. A*, rspa20110422.
- 745 Billings, S. E., and S. A. Kattenhorn (2005), The great thickness debate: Ice shell thickness
746 models for Europa and comparisons with estimates based on flexure at ridges, *Icarus*,
747 177(2), 397-412.
- 748 Blankenship, D. D., D. A. Young, W. B. Moore, and J. C. Moore (2009), Radar sounding of
749 Europa's subsurface properties and processes: The view from Earth, *Europa. University*
750 *of Arizona Press, Tucson, AZ*.
- 751 Board, S. S., and N. R. Council (2012), *Vision and voyages for planetary science in the decade*
752 *2013-2022*, National Academies Press.
- 753 Buffo, J., B. Schmidt, and C. Huber (2018), Multiphase reactive transport and platelet ice
754 accretion in the sea ice of McMurdo sound, Antarctica, *Journal of Geophysical Research:*
755 *Oceans*, 123(1), 324-345.
- 756 Butler, B. M., S. Papadimitriou, A. Santoro, and H. Kennedy (2016), Mirabilite solubility in
757 equilibrium sea ice brines, *Geochimica et Cosmochimica Acta*, 182, 40-54.
- 758 Carr, M. H., M. J. Belton, C. R. Chapman, M. E. Davies, P. Geissler, R. Greenberg, A. S.
759 McEwen, B. R. Tufts, R. Greeley, and R. Sullivan (1998), Evidence for a subsurface
760 ocean on Europa, *Nature*, 391(6665), 363.
- 761 Cassen, P., R. T. Reynolds, and S. Peale (1979), Is there liquid water on Europa?, *Geophysical*
762 *Research Letters*, 6(9), 731-734.
- 763 Charette, M. A., and W. H. Smith (2010), The volume of Earth's ocean, *Oceanography*, 23(2),
764 112-114.
- 765 Chyba, C. F., and C. B. Phillips (2001), Possible ecosystems and the search for life on Europa,
766 *Proceedings of the National Academy of Sciences*, 98(3), 801-804.
- 767 Commission, I. O. (2010), The International thermodynamic equation of seawater–2010:
768 calculation and use of thermodynamic properties.[includes corrections up to 31st October
769 2015].
- 770 Craven, M., I. Allison, H. A. Fricker, and R. Warner (2009), Properties of a marine ice layer
771 under the Amery Ice Shelf, East Antarctica, *Journal of Glaciology*, 55(192), 717-728.
- 772 Davis, N., and P. Wadhams (1995), A statistical analysis of Arctic pressure ridge morphology,
773 *Journal of Geophysical Research: Oceans*, 100(C6), 10915-10925.
- 774 Des Marais, D. J., J. A. Nuth III, L. J. Allamandola, A. P. Boss, J. D. Farmer, T. M. Hoehler, B.
775 M. Jakosky, V. S. Meadows, A. Pohorille, and B. Runnegar (2008), The NASA
776 astrobiology roadmap, *Astrobiology*, 8(4), 715-730.

- 777 Dickson, A. G., and C. Goyet (1994), Handbook of methods for the analysis of the various
778 parameters of the carbon dioxide system in sea water. Version 2*Rep.*, Oak Ridge National
779 Lab., TN (United States).
- 780 Durham, W., O. Prieto-Ballesteros, D. Goldsby, and J. Kargel (2010), Rheological and thermal
781 properties of icy materials, *Space Science Reviews*, 153(1-4), 273-298.
- 782 Eicken, H. (2003), From the microscopic, to the macroscopic, to the regional scale: growth,
783 microstructure and properties of sea ice, *Sea ice: an introduction to its physics, chemistry,*
784 *biology and geology*, 22-81.
- 785 Fagents, S. A. (2003), Considerations for effusive cryovolcanism on Europa: The post-Galileo
786 perspective, *Journal of Geophysical Research: Planets*, 108(E12).
- 787 Feltham, D., N. Untersteiner, J. Wettlaufer, and M. Worster (2006), Sea ice is a mushy layer,
788 *Geophysical Research Letters*, 33(14).
- 789 Galton-Fenzi, B., J. Hunter, R. Coleman, S. Marsland, and R. Warner (2012), Modeling the basal
790 melting and marine ice accretion of the Amery Ice Shelf, *Journal of Geophysical*
791 *Research: Oceans*, 117(C9).
- 792 Golden, K., S. Ackley, and V. Lytle (1998), The percolation phase transition in sea ice, *Science*,
793 282(5397), 2238-2241.
- 794 Golden, K. M., H. Eicken, A. Heaton, J. Miner, D. Pringle, and J. Zhu (2007), Thermal evolution
795 of permeability and microstructure in sea ice, *Geophysical Research Letters*, 34(16).
- 796 Greenberg, R., G. V. Hoppa, B. Tufts, P. Geissler, J. Riley, and S. Kadel (1999), Chaos on
797 Europa, *Icarus*, 141(2), 263-286.
- 798 Griewank, P. J., and D. Notz (2013), Insights into brine dynamics and sea ice desalination from a
799 1-D model study of gravity drainage, *Journal of Geophysical Research: Oceans*, 118(7),
800 3370-3386.
- 801 Han, L., and A. P. Showman (2005), Thermo-compositional convection in Europa's icy shell
802 with salinity, *Geophysical research letters*, 32(20).
- 803 Hand, K. P., and C. F. Chyba (2007), Empirical constraints on the salinity of the euroman ocean
804 and implications for a thin ice shell, *Icarus*, 189(2), 424-438.
- 805 Howell, S. M., and R. T. Pappalardo (2018), Band formation and ocean-surface interaction on
806 Europa and Ganymede, *Geophysical Research Letters*, 45(10), 4701-4709.
- 807 Huber, C., A. Parmigiani, B. Chopard, M. Manga, and O. Bachmann (2008), Lattice Boltzmann
808 model for melting with natural convection, *International Journal of Heat and Fluid Flow*,
809 29(5), 1469-1480.
- 810 Hunke, E., D. Notz, A. Turner, and M. Vancoppenolle (2011), The multiphase physics of sea ice:
811 a review for model developers, *The Cryosphere*, 5(4), 989-1009.
- 812 Johnson, B. C., R. Y. Sheppard, A. C. Pascuzzo, E. A. Fisher, and S. E. Wiggins (2017a),
813 Porosity and Salt Content Determine if Subduction Can Occur in Europa's Ice Shell,
814 *Journal of Geophysical Research: Planets*, 122(12), 2765-2778.
- 815 Johnson, B. C., R. Y. Sheppard, A. C. Pascuzzo, E. A. Fisher, and S. E. Wiggins (2017b),
816 Porosity and Salt Content Determine if Subduction Can Occur in Europa's Ice Shell,
817 *Journal of Geophysical Research: Planets*.
- 818 Kalousová, K., D. M. Schroeder, and K. M. Soderlund (2017), Radar attenuation in Europa's ice
819 shell: Obstacles and opportunities for constraining the shell thickness and its thermal
820 structure, *Journal of Geophysical Research: Planets*, 122(3), 524-545.

- 821 Kargel, J. S., J. Z. Kaye, J. W. Head III, G. M. Marion, R. Sassen, J. K. Crowley, O. P.
822 Ballesteros, S. A. Grant, and D. L. Hogenboom (2000), Europa's crust and ocean: origin,
823 composition, and the prospects for life, *Icarus*, 148(1), 226-265.
- 824 Kattenhorn, S. A. (2018), Commentary: The Feasibility of Subduction and Implications for Plate
825 Tectonics on Jupiter's moon Europa.
- 826 Kattenhorn, S. A., and L. M. Prockter (2014), Evidence for subduction in the ice shell of Europa,
827 *Nature Geoscience*, 7(10), 762.
- 828 Khazendar, A., E. Rignot, and E. Larour (2009), Roles of marine ice, rheology, and fracture in
829 the flow and stability of the Brunt/Stancomb-Wills Ice Shelf, *Journal of Geophysical*
830 *Research: Earth Surface*, 114(F4).
- 831 Khurana, K., M. Kivelson, D. Stevenson, G. Schubert, C. Russell, R. Walker, and C. Polanskey
832 (1998), Induced magnetic fields as evidence for subsurface oceans in Europa and
833 Callisto, *Nature*, 395(6704), 777.
- 834 Kivelson, M. G., K. K. Khurana, C. T. Russell, M. Volwerk, R. J. Walker, and C. Zimmer
835 (2000), Galileo magnetometer measurements: A stronger case for a subsurface ocean at
836 Europa, *Science*, 289(5483), 1340-1343.
- 837 Kurtz, N., and T. Markus (2012), Satellite observations of Antarctic sea ice thickness and
838 volume, *Journal of Geophysical Research: Oceans*, 117(C8).
- 839 Laxon, S. W., K. A. Giles, A. L. Ridout, D. J. Wingham, R. Willatt, R. Cullen, R. Kwok, A.
840 Schweiger, J. Zhang, and C. Haas (2013), CryoSat-2 estimates of Arctic sea ice thickness
841 and volume, *Geophysical Research Letters*, 40(4), 732-737.
- 842 Lyon, W. (1961), DIVISION OF OCEANOGRAPHY AND METEOROLOGY: OCEAN AND
843 SEA-ICE RESEARCH IN THE ARCTIC OCEAN VIA SUBMARINE, *Transactions of*
844 *the New York Academy of Sciences*, 23(8 Series II), 662-674.
- 845 Malmgren, F., and G. Institutt (1927), *On the properties of sea-ice*, AS John Griegs Boktrykkeri.
- 846 Manga, M., and C. Michaut (2017), Formation of lenticulae on Europa by saucer-shaped sills,
847 *Icarus*, 286, 261-269.
- 848 McCarthy, C., R. F. Cooper, D. L. Goldsby, W. B. Durham, and S. H. Kirby (2011), Transient
849 and steady state creep response of ice I and magnesium sulfate hydrate eutectic
850 aggregates, *Journal of Geophysical Research: Planets*, 116(E4).
- 851 McCarthy, C., R. F. Cooper, S. H. Kirby, K. D. Rieck, and L. A. Stern (2007), Solidification and
852 microstructures of binary ice-I/hydrate eutectic aggregates, *American Mineralogist*,
853 92(10), 1550-1560.
- 854 McCord, T. B., G. B. Hansen, D. L. Matson, T. V. Johnson, J. K. Crowley, F. P. Fanale, R. W.
855 Carlson, W. D. Smythe, P. D. Martin, and C. A. Hibbitts (1999), Hydrated salt minerals
856 on Europa's surface from the Galileo near-infrared mapping spectrometer (NIMS)
857 investigation, *Journal of Geophysical Research: Planets*, 104(E5), 11827-11851.
- 858 McCord, T. B., G. Teeter, G. B. Hansen, M. T. Sieger, and T. M. Orlando (2002), Brines
859 exposed to Europa surface conditions, *Journal of Geophysical Research: Planets*,
860 107(E1), 4-1-4-6.
- 861 McKinnon, W. B. (1999), Convective instability in Europa's floating ice shell, *Geophysical*
862 *Research Letters*, 26(7), 951-954.
- 863 Michaut, C., and M. Manga (2014), Domes, pits, and small chaos on Europa produced by water
864 sills, *Journal of Geophysical Research: Planets*, 119(3), 550-573.

- 865 Mitri, G., and A. P. Showman (2005), Convective–conductive transitions and sensitivity of a
866 convecting ice shell to perturbations in heat flux and tidal-heating rate: Implications for
867 Europa, *Icarus*, 177(2), 447-460.
- 868 Nakawo, M., and N. K. Sinha (1981), Growth rate and salinity profile of first-year sea ice in the
869 high Arctic, *Journal of Glaciology*, 27(96), 315-330.
- 870 Nakawo, M., and N. K. Sinha (1984), A note on brine layer spacing of first-year sea ice,
871 *Atmosphere-ocean*, 22(2), 193-206.
- 872 Nimmo, F., and E. Gaidos (2002), Strike-slip motion and double ridge formation on Europa,
873 *Journal of Geophysical Research: Planets*, 107(E4), 5-1-5-8.
- 874 Nimmo, F., B. Giese, and R. Pappalardo (2003), Estimates of Europa's ice shell thickness from
875 elastically-supported topography, *Geophysical Research Letters*, 30(5).
- 876 Notz, D., and M. G. Worster (2009), Desalination processes of sea ice revisited, *Journal of*
877 *Geophysical Research: Oceans*, 114(C5).
- 878 Pappalardo, R., M. Belton, H. Breneman, M. Carr, C. Chapman, G. Collins, T. Denk, S. Fagents,
879 P. Geissler, and B. Giese (1999), Does Europa have a subsurface ocean? Evaluation of
880 the geological evidence, *Journal of Geophysical Research: Planets*, 104(E10), 24015-
881 24055.
- 882 Pappalardo, R. T., and A. C. Barr (2004), The origin of domes on Europa: The role of thermally
883 induced compositional diapirism, *Geophysical Research Letters*, 31(1).
- 884 Phillips, C. B., and R. T. Pappalardo (2014), Europa Clipper mission concept: Exploring Jupiter's
885 ocean moon, *Eos, Transactions American Geophysical Union*, 95(20), 165-167.
- 886 Reynolds, R. T., S. W. Squyres, D. S. Colburn, and C. P. McKay (1983), On the habitability of
887 Europa, *Icarus*, 56(2), 246-254.
- 888 Ross, M., and G. Schubert (1987), Tidal heating in an internal ocean model of Europa, *Nature*,
889 325(6100), 133-134.
- 890 Rubinštejn, L. (2000), *The stefan problem*, American Mathematical Soc.
- 891 Russell, M. J., A. E. Murray, and K. P. Hand (2017), The possible emergence of life and
892 differentiation of a shallow biosphere on irradiated icy worlds: the example of Europa,
893 *Astrobiology*, 17(12), 1265-1273.
- 894 Schmidt, B. E., D. D. Blankenship, G. W. Patterson, and P. M. Schenk (2011), Active formation
895 of 'chaos terrain' over shallow subsurface water on Europa, *Nature*, 479(7374), 502-505,
896 doi:10.1038/nature10608.
- 897 Soderlund, K., B. Schmidt, J. Wicht, and D. Blankenship (2014), Ocean-driven heating of
898 Europa's icy shell at low latitudes, *Nature Geoscience*, 7(1), 16.
- 899 Sparks, W. B., B. E. Schmidt, M. A. McGrath, K. P. Hand, J. Spencer, M. Cracraft, and S. E.
900 Deustua (2017), Active cryovolcanism on Europa?, *The Astrophysical Journal Letters*,
901 839(2), L18.
- 902 Squyres, S. W., R. T. Reynolds, P. M. Cassen, and S. J. Peale (1983), Liquid water and active
903 resurfacing on Europa, *Nature*, 301(5897), 225-226.
- 904 Tobie, G., G. Choblet, and C. Sotin (2003), Tidally heated convection: Constraints on Europa's
905 ice shell thickness, *Journal of Geophysical Research: Planets*, 108(E11).
- 906 Turner, A. K., and E. C. Hunke (2015), Impacts of a mushy-layer thermodynamic approach in
907 global sea-ice simulations using the CICE sea-ice model, *Journal of Geophysical*
908 *Research: Oceans*, 120(2), 1253-1275.

- 909 Turner, A. K., E. C. Hunke, and C. M. Bitz (2013), Two modes of sea-ice gravity drainage: A
910 parameterization for large-scale modeling, *Journal of Geophysical Research: Oceans*,
911 *118*(5), 2279-2294.
- 912 Vance, S., K. Hand, and R. Pappalardo (2016), Geophysical controls of chemical disequilibria in
913 Europa, *Geophysical Research Letters*, *43*(10), 4871-4879.
- 914 Walker, C., and B. Schmidt (2015), Ice collapse over trapped water bodies on Enceladus and
915 Europa, *Geophysical Research Letters*, *42*(3), 712-719.
- 916 Weeks, W. F., and S. F. Ackley (1986), The growth, structure, and properties of sea ice, in *The*
917 *geophysics of sea ice*, edited, pp. 9-164, Springer.
- 918 Wells, A., J. Wettlaufer, and S. Orszag (2011), Brine fluxes from growing sea ice, *Geophysical*
919 *Research Letters*, *38*(4).
- 920 Worster, M. G., and D. W. Rees Jones (2015), Sea-ice thermodynamics and brine drainage,
921 *Philosophical Transactions of the Royal Society A: Mathematical, Physical and*
922 *Engineering Sciences*, *373*(2045), 20140166.
- 923 Zolotov, M. Y., and J. Kargel (2009), *On the chemical composition of Europa's icy shell, ocean,*
924 *and underlying rocks*, University of Arizona Press Tucson, AZ.
- 925 Zolotov, M. Y., and E. L. Shock (2001), Composition and stability of salts on the surface of
926 Europa and their oceanic origin, *Journal of Geophysical Research: Planets*, *106*(E12),
927 32815-32827.
- 928 Zotikov, I. A., V. S. Zagorodnov, and J. V. Raikovsky (1980), Core drilling through the Ross Ice
929 Shelf (Antarctica) confirmed basal freezing, *Science*, *207*(4438), 1463-1465.
- 930